

Experimental study on cyclic behavior of composite beam with corrugated steel web considering different shear-span ratio

Wang, Sihao; Liu, Yuqing; He, Jun; Xin, Haohui; Yao, Hongbing

DOI

[10.1016/j.engstruct.2018.11.044](https://doi.org/10.1016/j.engstruct.2018.11.044)

Publication date

2019

Document Version

Final published version

Published in

Engineering Structures

Citation (APA)

Wang, S., Liu, Y., He, J., Xin, H., & Yao, H. (2019). Experimental study on cyclic behavior of composite beam with corrugated steel web considering different shear-span ratio. *Engineering Structures*, 180, 669-684. <https://doi.org/10.1016/j.engstruct.2018.11.044>

Important note

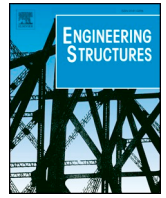
To cite this publication, please use the final published version (if applicable). Please check the document version above.

Copyright

Other than for strictly personal use, it is not permitted to download, forward or distribute the text or part of it, without the consent of the author(s) and/or copyright holder(s), unless the work is under an open content license such as Creative Commons.

Takedown policy

Please contact us and provide details if you believe this document breaches copyrights. We will remove access to the work immediately and investigate your claim.



Experimental study on cyclic behavior of composite beam with corrugated steel web considering different shear-span ratio

Sihao Wang^a, Yuqing Liu^a, Jun He^{b,*}, Haohui Xin^c, Hongbing Yao^d

^a Department of Bridge Engineering, Tongji University, Shanghai, China

^b School of Civil Engineering, Changsha University of Science & Technology, Hunan, China

^c Civil Engineering and Geosciences, Delft University and Technology, Netherlands

^d Sichuan Highway Design and Research Institute, Sichuan, China

ARTICLE INFO

Keywords:

Composite beam
Corrugated steel web
Shear-span ratio
Cyclic behavior
Quasi-static test

ABSTRACT

This paper proposes an innovative use of corrugated steel plates as the webs of the crossbeam in the tower of a suspension bridge to get better seismic performance. Three 1/4-scaled models of composite beam with corrugated steel webs considering different shear-span ratio were fabricated to conduct quasi-static test. The structural behaviors including failure modes, hysteretic curves, ductility, strength and stiffness degradation, energy dissipation capacity, deformation recovery ability, shear force distribution and strain responses were investigated. Test results indicate that the specimen with large shear-span ratio presents ductile flexural failure, and the hysteretic curve is stable and plump with slight pinching, which indicates good energy dissipation performance. However, the specimen with small shear-span ratio fails due to brittle shear buckling of corrugated steel web, showing remarkable pinching phenomenon and poor hysteretic behavior. With the increase of shear-span ratio, the load-carrying capacity and lateral initial stiffness are reduced, but the ductility and energy dissipation ability are improved significantly. The energy dissipation capacity of such composite beam is better than that of the RC structures, the strength degradation is slight for the specimen with a proper shear-span ratio, and the deformation recovery ability is good for all test specimens. The corrugated steel web carries about 80% of the shear force and shear stress uniformly distributed along the web height. The test results demonstrate that the composite beam with corrugated steel web of a reasonable shear-span ratio can be applied in anti-seismic structure with superior energy dissipation performance. In addition, simplified formulas were proposed to evaluate the flexural strength and shear buckling strength of a composite beam with corrugated steel webs, the calculated results agree well with the test results, verifying the accuracy of these proposed formulas.

1. Introduction

In recent years, the corrugated steel plates have been increasingly applied in infrastructure construction, such as bridges, shear walls, and industrial buildings etc. In comparison to a conventional flat steel plate, the corrugated steel profile without additional longitude or transverse stiffeners shows higher out-of-plane stiffness and in-plane shear strength. One of the most common applications for corrugated steel plates in bridge engineering is an alternative to concrete webs in box-girder bridges [1]. Compared with conventional concrete webs, the self-weight of corrugated steel webs is greatly reduced, and because of the low axial stiffness of the corrugated plates, prestressing can be efficiently introduced into concrete flanges, also the influences of concrete creep and shrinkage, temperature variation to composite girder can be alleviated effectively. Thus, the strength, stability of the structure, and

material efficiency can be improved by concrete flanges combined with corrugated steel webs.

An innovative application of the corrugated steel plates is to replace the concrete webs of the crossbeam in the tower of a suspension bridge to get better seismic performance. Because of the large weight and stiffness of traditional concrete crossbeam in the tower of a suspension bridge, shear and flexural failure are easy to occur at the connection area between pylon and crossbeam under seismic loading. In order to reduce the self-weight and axial stiffness of crossbeam, steel-concrete composite box beams with corrugated steel webs were adopted as the crossbeams in the tower of Xingkang Dadu River Bridge in Luding [2], as shown in Fig. 1. The crossbeam was composed of four corrugated steel webs, top and bottom concrete slabs. The corrugated steel webs and top concrete slab were connected by twin Perfo-Bond Strip (PBL) connectors. The embedded connectors [3] were adopted between

* Corresponding author.

E-mail address: hejun@csust.edu.cn (J. He).

<https://doi.org/10.1016/j.engstruct.2018.11.044>

Received 6 February 2018; Received in revised form 12 October 2018; Accepted 15 November 2018

Available online 04 December 2018

0141-0296/ © 2018 Elsevier Ltd. All rights reserved.

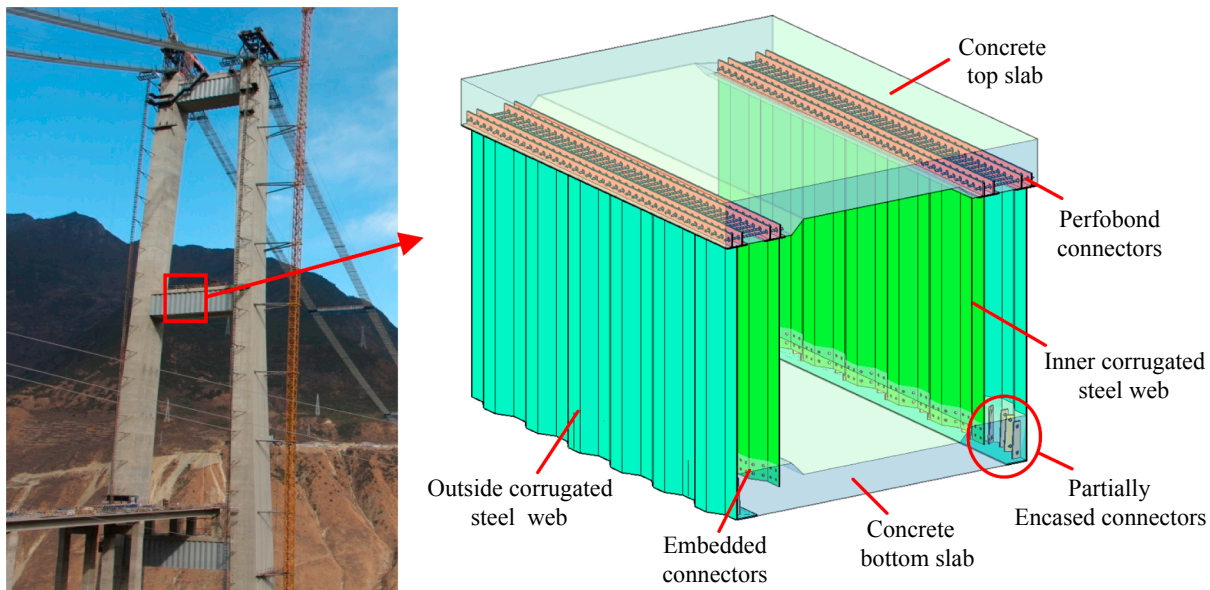


Fig. 1. The crossbeam with corrugated steel webs of Xingkang Dadu River Bridge.

corrugated steel webs and bottom concrete slabs. The application of corrugated steel webs can reduce the seismic response of the crossbeam due to self-weight reduction, and it is also expected to improve the energy dissipation and deformation capacity due to the “accordion effect” of corrugated panels.

Considerable researches have been conducted on the static behavior of steel or composite girder with corrugated steel webs including bending, shear, torsional and fatigue [4–17], but relatively limit studies related to seismic behavior. Mo et al. [18] reported an experiment on framed shear walls made of corrugated steel plates, the influences of the reinforced concrete frame and the thickness of corrugated steel plate on their utility were analyzed, also the improved seismic performance of such structure was verified. Shimizu et al. [19] performed an experimental study on a full-scale load-bearing wall using corrugated steel sheets; it was found that corrugated shear diaphragms could increase the seismic performance of steel-framed houses. Emami et al. [20,21] conducted an experimental research on the cyclic behavior of trapezoidally corrugated steel shear walls and unstiffened steel shear walls, finite element explicit dynamic analyses including both material and geometric nonlinearities were employed for cyclic loading tests. The experimental and numerical results revealed that the energy dissipation capacity, ductility ratio, out of plane stiffness and the elastic shear strength of the corrugated specimens were all higher than that of the unstiffened specimen. Bahrebar et al. [22] presented a numerical study on the structural performance of trapezoidally corrugated steel shear walls, the effects of web plate thickness, corrugation angle on the cyclic behavior and energy absorption capabilities were analyzed. Farzampour et al. [23] conducted a detailed finite element analysis of steel plate and corrugated steel plate shear walls considering numerous variable parameters and concluded that corrugated panels improve the ultimate strength and postpone degradation point which leads to better behavior under cyclic loading. Aydın et al. [24,25] tested beam-to-column connections with flat plate and corrugated plate under cyclic loading, the results showed that panel zones with thicker flat plate were more stable than those with corrugated plates, but the diagonally-stiffened connections with corrugated plate exhibited comparable behavior to flat plate panel zones. Shahmohammadi et al. [26] proposed the application of corrugated plates as the web of steel coupling beams, and nonlinear finite element (FE) analyses were performed considering the shape of web plate, web thickness, number of corrugations and corrugation angle. The application of a corrugated web makes it possible to improve rotational capacity compared with conventional steel coupling

beams. Hajsadeghi et al. [27] investigated the energy dissipation characteristics of steel coupling beams with corrugated webs using numerical simulations and demonstrated that steel coupling beams with corrugated webs possess appropriate energy absorption capacity and are capable of dissipating the input energy in a quite desirable and efficient manner.

Based on above-mentioned references, corrugated steel plates exhibit better seismic performance, but these researches mainly focus on steel structures, e.g. steel shear wall, steel coupling beams, and so on, few studies on the seismic behavior of composite beam as the crossbeam in bridge tower were reported as far as the authors’ knowledge. Moreover, the seismic behavior of corrugated steel plate is quite different from the composite beam with corrugated steel webs due to the restraining effect of concrete slabs which connected the corrugated steel plate by shear connectors. Therefore, it is necessary to investigate seismic behavior of composite beam with corrugated steel webs.

This paper aims to determine the seismic behavior of composite beam with corrugated steel webs through quasi-static tests on three specimens with different shear-span ratios. The damage process and failure modes, hysteretic curves, load-carrying capacity and ductility, strength and stiffness degradation, energy dissipation capacity, deformation recovery ability were obtained and analyzed. In addition, the influences of shear-span ratio on the seismic performance of the test specimens were compared. All the findings from present investigation will provide a reference for seismic design and the application of composite crossbeam with corrugated steel webs.

2. Experimental program

2.1. Test specimens

In order to investigate and distinguish the cyclic behavior of proposed composite crossbeam with corrugated steel webs, totally three 1/4 scaled specimens with different shear-span ratios (denoted as CSW-1, CSW-2, and CSW-3) were designed and constructed. All the specimens with I-shaped cross section include top and bottom concrete slabs, and corrugated steel web. In addition, an RC basement with enough stiffness was designed to simulate the rigid connection between the composite beam and pylon or end diaphragm.

All test specimens have the same cross-section but different height. Fig. 2 shows the structural dimensions and reinforcements’ arrangement, where h is the effective height from the top of the basement to the

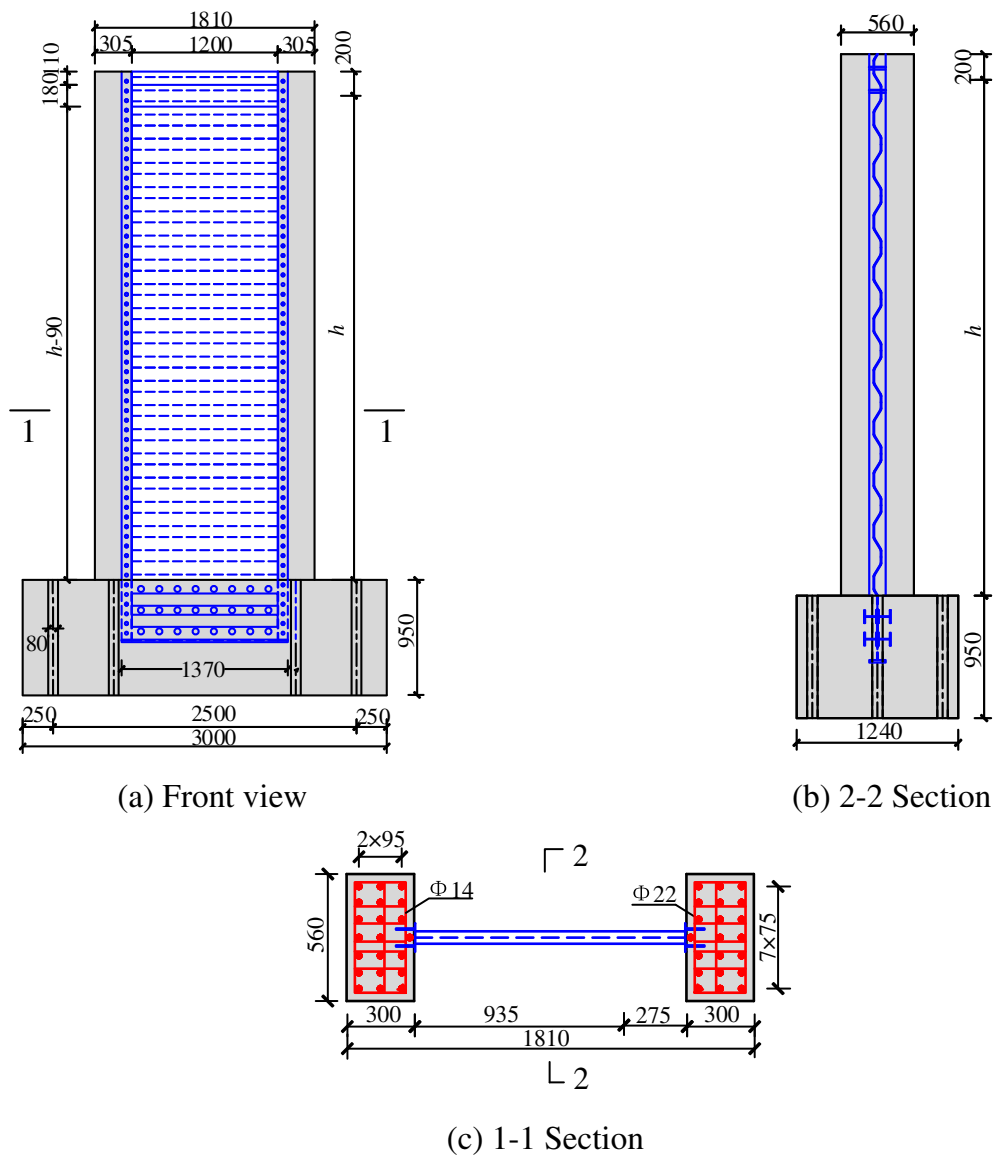


Fig. 2. Structural dimensions and reinforcements arrangement of test specimens (unit: mm).



Fig. 3. Test specimens.

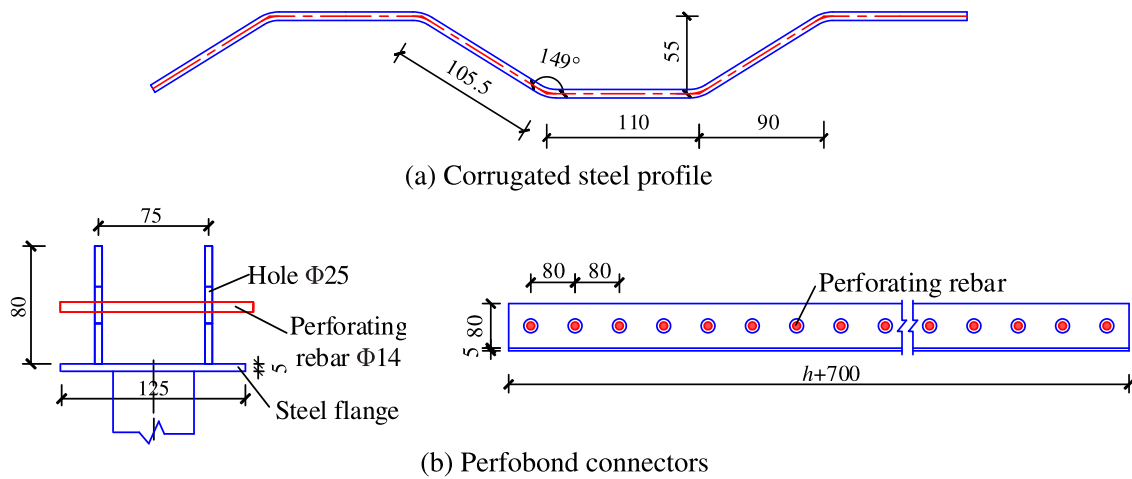


Fig. 4. Details of corrugated steel profile and shear connectors (unit: mm).

lateral loading point. The effective heights were 2000 mm, 3000 mm, and 4000 mm for specimens CSW-1, CSW-2, and CSW-3 respectively. The depth of the composite beam was 1810 mm, in which the thickness and width of concrete slabs were 300 mm and 560 mm, respectively, while the depth of the corrugated steel beam was 1210 mm. So, the shear-span ratio (height/depth) of specimens CSW-1, CSW-2, and CSW-3 were 1.11, 1.67 and 2.22, respectively. The corrugated steel beam was inserted into a RC basement (length \times width \times depth: 3000 mm \times 1240 mm \times 950 mm), three rows of PBL connectors were used to combine the steel beam and basement. As for the arrangement of longitudinal reinforcements in concrete slabs, three rows and seven columns of 22 mm-diameter reinforcements were installed with a spacing of 95 mm in depth direction and 75 mm in width direction respectively. In addition, stirrups with a diameter of 14 mm and a spacing of 80 mm were applied in the longitudinal direction. Two vertical stiffeners with a thickness of 25 mm were welded on both sides of the steel web at the loading position to avoid local buckling; the distance between these two stiffeners was 180 mm. The photos of test specimens after fabrication are presented in Fig. 3.

Fig. 4 shows the details of corrugated steel profile, shear connectors between the corrugated steel beam and concrete slabs. The unit wavelength of the corrugated web was 400 mm, in which the width of both horizontal and inclined panel was 110 mm, and the projected width of the inclined panel was 90 mm, the corrugation depth was 55 mm, and the thickness of corrugated web was 6 mm. Two perforated steel plates with a transverse spacing of 75 mm were welded at the top and bottom steel flanges as PBL shear connectors to connect concrete slabs, the spacing between adjacent perforating holes in the longitudinal direction was 80 mm. The width and thickness of the steel flange were 125 mm and 5 mm respectively, and the diameter of perforated holes and penetrating rebar were 25 mm and 14 mm, respectively.

2.2. Material properties

The concrete used in these specimens had a nominal cubic compressive strength of 50 MPa. Three concrete cubes with a dimension of 150 \times 150 \times 150 mm and three prisms with a size of 150 \times 150 \times 300 mm were prepared at the same time as these test specimens constructed, and they were cured for 28 days to test material properties according to GB-50010 [28]. The measured cube compressive strength f_{cu} , prismatic compressive strength $f_{c,pr}$, and Young's modulus E_c are given in Table 1. The steel beams were made of steel Q345qD with a nominal yielding stress of 345 MPa, and reinforcements in concrete slabs adopted steel HRB335 with a nominal yielding stress of 335 MPa. The measured tensile yielding stress (f_y), ultimate stress (f_u), and Young's modulus (E_s) of steel plate and steel reinforcement are

Table 1

Mechanical properties of concrete.

Specimen	Cube compressive strength f_{cu} (MPa)	Prismatic compressive strength $f_{c,pr}$ (MPa)	Young's modulus E_c (10^4 MPa)
No. 1	60.4	49.7	3.37
2	61.8	60.9	3.35
3	57.6	57.7	3.37
Average	59.9	56.1	3.36

Table 2

Mechanical properties of steel plates and reinforcements.

Components	Thickness or diameter /mm	Yielding stress f_y /MPa	Ultimate stress f_u /MPa	Young's modulus E_s /GPa
Corrugated steel plates	6	420.0	538.0	193.9
Stiffeners	25	393.0	523.0	203.1
Perforated plate	5	415.0	533.0	204.8
Steel flange	5	415.0	533.0	204.8
Steel stirrups	$\phi 14$	505.0	650.0	202.8
Longitudinal rebar	$\phi 22$	475.0	615.0	202.4

presented in Table 2.

2.3. Test setup and loading program

Quasi-static tests of composite beams with corrugated steel web were carried out in Structure Laboratory of Sichuan Highway Design and Research Institute (SCHDRI), the test setup is illustrated in Fig. 5. The free end of the test specimen was clamped to a horizontal hydraulic actuator with a maximum loading capacity of 5000 kN. The hydraulic actuator was connected to the reaction wall, which was responsible for applying the cyclic lateral loads to test specimens. The basement was anchored to the strong floor of the laboratory by high strength bolts. In addition, two steel beams at the top of the basement and two steel blocks at both sides of the basement were installed to prevent up-lift and lateral movement of the basement.

Prior to the formal test, a preloading with 40 kN was conducted to check the good contact between the support and loading equipment, and to ensure the reliability of all the test equipment and the workability of all the measurement instruments. After preloading, the lateral loading was applied to the test specimen by hybrid force-control and displacement-control method, as shown in Fig. 6.

The loading process was divided into three stages. Firstly, before

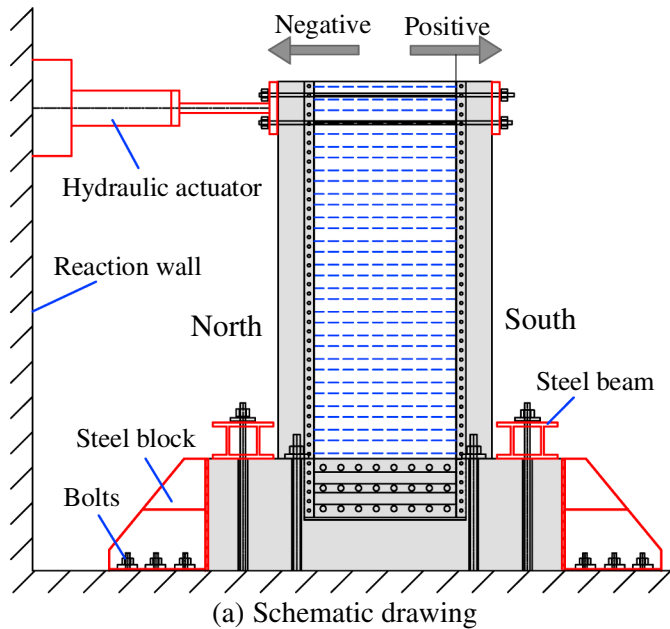


Fig. 5. Test setup.

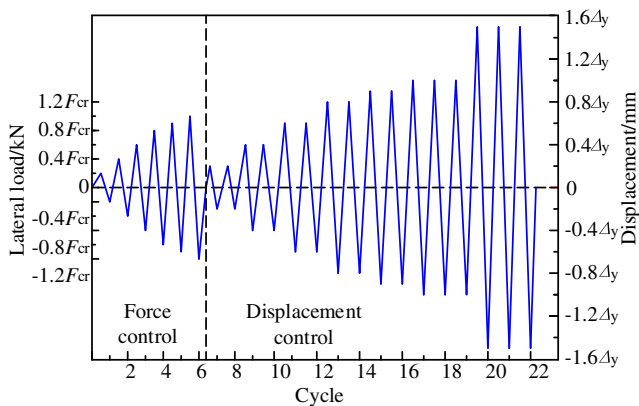


Fig. 6. Quasi-static loading procedure.

estimated concrete through crack load F_{cr} according to numerical analysis, increasing the load of $0.2 F_{cr}$ until to 80% of F_{cr} , after that the loading level changed to $0.1 F_{cr}$ until to F_{cr} , in this stage, the lateral load was controlled by force and one cycle was adopted at each loading level. Secondly, before yielding of longitudinal steel reinforcement, loading was controlled by displacement and repeated twice at each loading level. In this stage, the displacement was increased by 0.2 times of estimate yielding displacement Δ_y until to 80% of Δ_y , afterward, the displacement increment changed to $0.1 \Delta_y$ until to yielding of longitudinal steel reinforcement. Thirdly, after steel reinforcement yielding, loading was still controlled by displacement, and displacement loading was increased by 0.5 times of yielding displacement Δ_y until the lateral load dropped to about 85% of the peak load, each loading level repeated three times.

2.4. Instruments

The Instrumentation of test specimen consists of load cells, linear variable displacement transducers (LVDTs) and strain gauges. The lateral load applied to the test specimen was measured by load cells. The arrangement of LVDTs for specimen CSW-3 is shown in Fig. 7(a). The LVDTs W1, W2, and W3 were installed at the loading position to measure lateral displacement. The potential lateral slippage and

vertical uplift of the basement were measured by W4, W5, and W6. The LVDTs W7 and W8 measured the out of plane deformation of corrugated steel web during the loading process. The relative slip between the concrete slab and corrugated steel web at the free and fixed end of the specimen was also monitored by H1–H4 at the concrete-steel interface. At critical sections, strain gauges were mounted to measure the strain of corrugated steel web, steel flange, longitudinal reinforcements and stirrups during cyclic loading. The arrangement of these strain gauges for specimen CSW-3 is depicted in Fig. 7(b). The arrangements of LVDTs and strain gauges of other specimens are similar to specimen CSW-3.

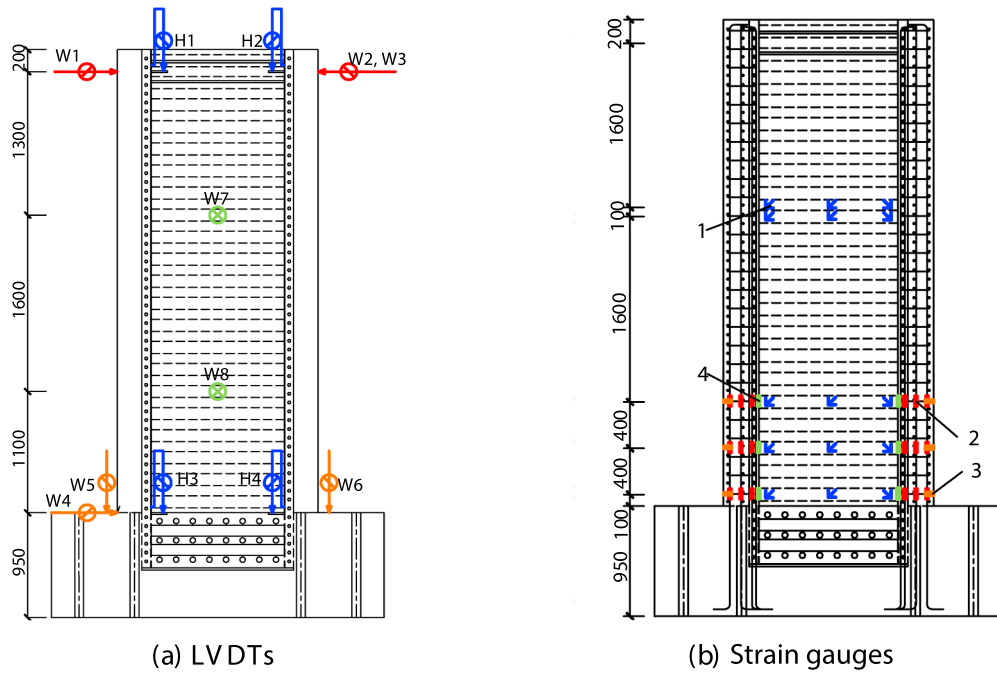
Besides the measurements of displacements and strains for test specimens during the loading process, cracking initiation and propagation on concrete surfaces were observed. All the information obtained from the transducers, gauges, and load cells were automatically recorded by a data acquisition system at regular intervals during the test.

3. Experimental phenomenon of specimens' behavior during loading

3.1. Specimen CSW-1

An initial flexural crack appeared on the surface of the concrete slab at the northern fixed end under loading of 150 kN. Then, new cracks were continuously generated, and the initial crack extended to both the east and west sides with increased loading cycles. When the applied load was increased to 400 kN, the initial crack propagated through the entire concrete slab, subsequently, the force-controlled loading was converted to displacement-controlled one.

With the increase of displacement amplitude in the subsequent cycles, lateral cracks developed fast from the fixed end to the free end of the test specimen, and most of these cracks were flexural cracks propagated in the lateral direction, as shown in Fig. 8(b). The yielding of longitudinal reinforcement in concrete slab occurred under displacement loading of 30 mm. In the subsequent lateral displacement of 45 mm, the specimen reached ultimate loading capacity. By the following reverse loading, the overall buckling of steel web appeared at the center of test specimen accompanied with several loud bangs and a significant tension field formed at approximately 45° to the lateral direction when the displacement reached to 30.8 mm, as shown in



- 1—Strain gauges on the corrugated steel web
- 2—Strain gauges on the longitudinal reinforcements
- 3—Strain gauges on the stirrups
- 4—Strain gauges on the steel flanges

Fig. 7. Instrumentation of the specimen CSW-3.

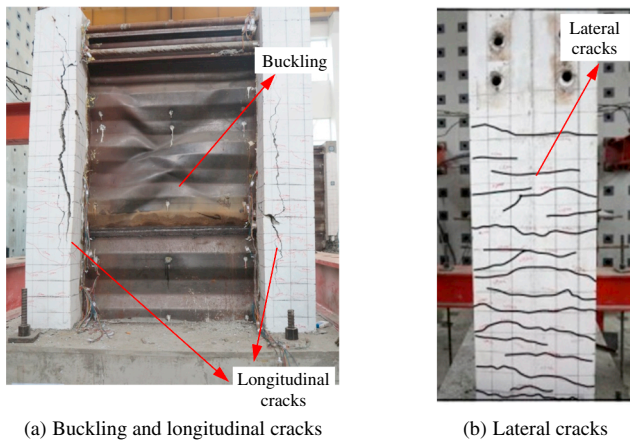


Fig. 8. Failure mode of CSW-1.

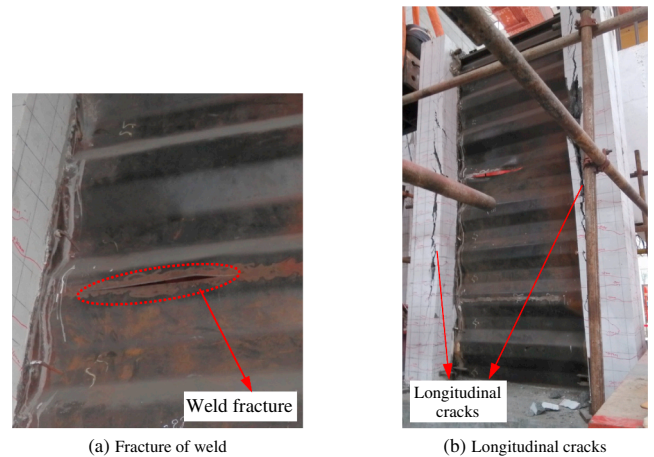


Fig. 9. Failure mode of CSW-2.

Fig. 11(a). At the same time, taking the buckling location as the starting height, a longitudinal crack extended upward in tension slab (north side) while another extended downward in compression slab (south side). By the following reverse loading, another tension field formed in the opposite direction, and longitudinal cracks at both concrete slabs also extended to the opposite direction, as illustrated in Fig. 11. Finally, the residual out-of-plane deformation of the corrugated steel web presented “X” shape, and longitudinal cracks appeared on both sides of concrete slabs. Then, load carrying capacity and displacement amplitude were decreased; therefore, the loading was terminated. Finally, the crack pattern and failure mode of specimen CSW-1 are shown in Fig. 8.

3.2. Specimen CSW-2

An initial lateral crack appeared on the surface of the concrete slab at the northern fixed end during loading level of 120 kN. Then, new cracks continuously occurred, and the initial crack extended to both east and west sides with the increment of loading level. When the applied load was increased to 400 kN, the initial crack propagated through the entire concrete slab, afterward, displacement-controlled loading was applied instead of force-controlled loading.

By continuing displacement loading, the crack development of specimen CSW-2 was similar to that of CSW-1. When the applied displacement increased to 42 mm, longitudinal reinforcement in tensile

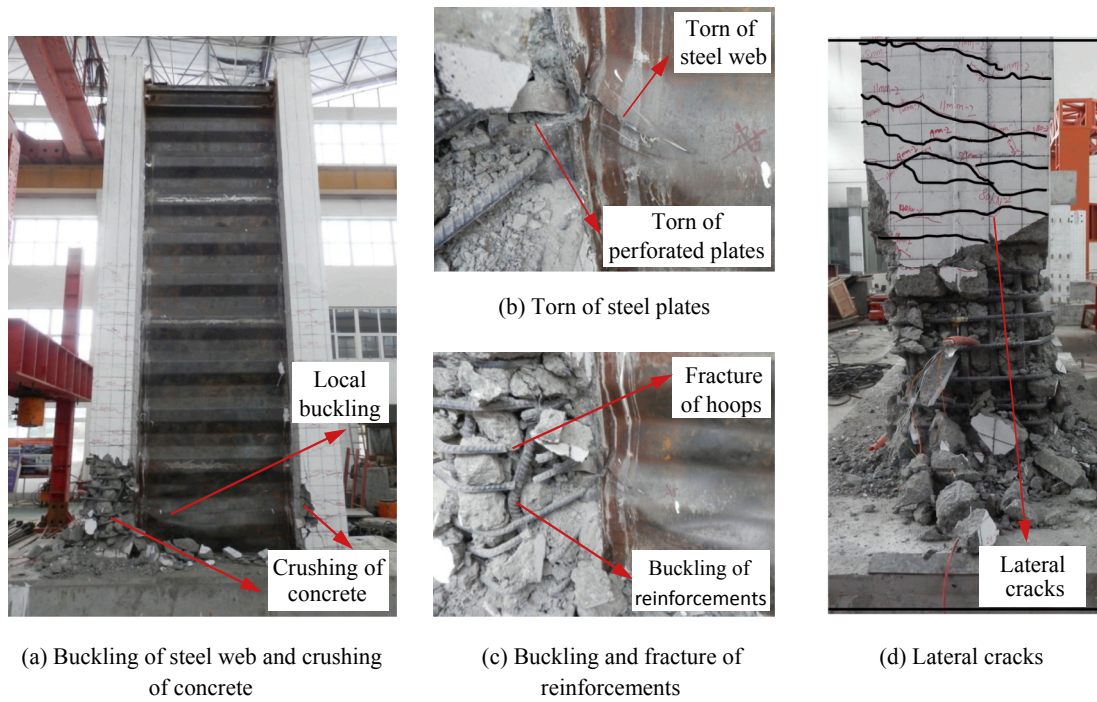


Fig. 10. Failure mode of CSW-3.

concrete slab yielded. With increasing displacement to 47 mm, unexpected fracture of welding between corrugated steel panels occurred, resulting in abruptly falling of load-carrying capacity of the specimen. Then, longitudinal cracks appeared and propagated in both concrete slabs, which were similar to specimen CSW-1. In the subsequent loading cycle, the fracture length of the welding was continuously extended, and longitudinal cracks almost propagated through whole height of the test specimen, finally the specimen loss its load-carrying capacity. The final failure mode of test specimen CSW-2 is shown in Fig. 9.

3.3. Specimen CSW-3

An initial lateral crack appeared on the surface of the concrete flange at the northern fixed end under loading of 80 kN. Then, new

cracks were continuously observed, and the initial crack extended to both east and west sides during loading cycles. When the applied load was increased to 160 kN, the initial crack propagated through the entire concrete slab, and then the force-controlled loading was changed to displacement-controlled loading.

With the increase of displacement amplitude, the crack development of test specimen CSW-3 was similar to that of CSW-1. Under applied displacement of 43 mm, longitudinal reinforcement in tensile concrete slab yielded. Afterward, the loading capacity continued to increase with applied lateral displacement. When the lateral displacement increased to 102 mm, the specimen reached ultimate loading capacity, and obvious out-of-plane deformation occurred on corrugated steel web around the fixed end section. During the subsequent loading cycles, the perforated steel plates, steel flange and corrugated steel web

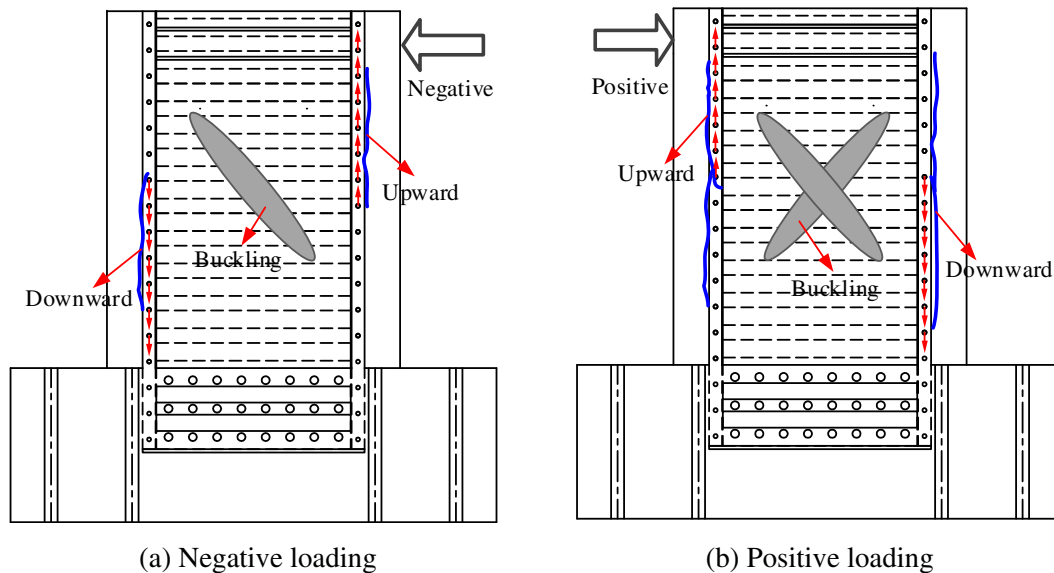


Fig. 11. Development of longitudinal cracks for CSW-1 and CSW-2.

near tensile concrete slab were torn around the fixed end of the test specimen, as shown in Fig. 10(b). In addition, crushing and spalling of concrete cover were detected. When the lateral displacement increased to 142 mm, concrete cover spalled off completely near the basement, leading to the expose of the hoops and longitudinal reinforcements. Under the subsequent loading cycle, the fracture of the hoops was observed, and core concrete between the hoops was crushed, accompanied by the bulking of the longitudinal reinforcements and steel web, as shown in Fig. 10(c). The failure mode of test specimen CSW-3 is illustrated in Fig. 10.

3.4. Comparison of the failure process

From the loading process and failure modes of test specimens with different shear-span ratios, it can be found that the failure was controlled by shear buckling of the corrugated steel web, fracture of the welding, flexural failure of the concrete slabs. The initial crack loading decreases with the increasing of shear-span ratio.

As for test specimen CSW-1, global buckling of the corrugated steel web caused the loss of its shearing capacity, which shows obvious brittle failure characteristic. The failure mechanism of test specimen CSW-2 was similar to that of CSW-1, unexpected welding fracture of the corrugated steel web resulting in the loss of shearing capacity, which also led to a sudden failure of this specimen. For the crossbeams of a suspension bridge tower or bridge girders with corrugated steel webs, the steel webs between adjacent segments are usually connected by welding on the construction site. Under complicated environmental conditions in the field, the quality of the weld is not easy to guarantee, which may become a weak point when subjected to seismic loading. Therefore, special attention should be paid to the welding quality or adding bolt connections between adjacent corrugated web segments to avoid brittle welding failure. Test specimen CSW-3 exhibited a typical bending failure, accompanied by concrete crushing, steel flange fracture, and buckling of longitudinal reinforcements and corrugated steel web, which experienced a ductile failure.

Another obvious damage characteristic for test specimens CSW-1 and CSW-2 is longitudinal cracks occurred on both concrete slabs, as depicted in Fig. 11. These cracks initiated at the same time as shear buckling or welding fracture of corrugated steel web, the steel web loss its shearing capacity, and relative slip between PBL connectors and concrete slabs increased rapidly. With subsequently applied load, relative slip increased obviously above the buckled section in the tensile slab, and longitudinal cracks propagated upward in the tensile slab, while longitudinal cracks developed downward in the compression slab.

4. Experimental results and discussion

4.1. Hysteretic curves

The hysteretic curves of test specimens are described in Fig. 12. It is observed that hysteretic curves can be divided into three stages: elastic, elastic-plastic and failure. The lateral loading and displacement are basically in linear relation at the elastic stage, loading and unloading curves are almost coincident, which indicates that the residual deformation after unloading can be negligible and the energy dissipation capacity is low at this stage. In the elastic-plastic stage, hysteretic curves show obvious nonlinearity, the slope of hysteretic curves decrease gradually with the increase of displacement amplitude. The displacement cannot return back to original position after unloading, showing an obvious residual deformation. Besides, the energy dissipation capacity was enhanced gradually at the elastic-plastic stage. At the failure stage, the stiffness decreased significantly due to cumulative damage of the test specimens, but the structures can still dissipate energy due to large deformations.

For test specimen CSW-1 with the smallest shear-span ratio, the

hysteretic curve was less plentiful, presenting reverse “Z” shape, load-carrying capacity and stiffness decreased rapidly after shear buckling of corrugated steel web, and the deformation ability and energy dissipation ability were relatively poor. As for test specimen CSW-3 with the largest shear-span ratio, the hysteretic curve was stable and plentiful, showing spindle shape, and the plastic deformation and energy dissipation ability are excellent. Test specimen CSW-2 just experienced the elastic stage because of the sudden welding fracture of the corrugated steel web.

The hysteretic curves of these three specimens exhibit different degrees of the pinching phenomenon. On one hand, relative slip between PBL connectors and concrete slabs, as well as at the interface between concrete and reinforcements, occurred with applied lateral load, however, the relative slip cannot be completely recovered after unloading. On the other hand, concrete cracks continued to open and close during the cyclic loading process, resulting in stiffness degradation. The pinching phenomenon of test specimen CSW-1 is more severe than that of test specimens CSW-2 and CSW-3, which indicates that the smaller of shear-span ratio, the more relative slip between steel and concrete. In addition, relatively stable hysteretic curves with slight pinching are indicative of good hysteretic performance for test specimen CSW-3.

4.2. Load-carrying capacity and ductility

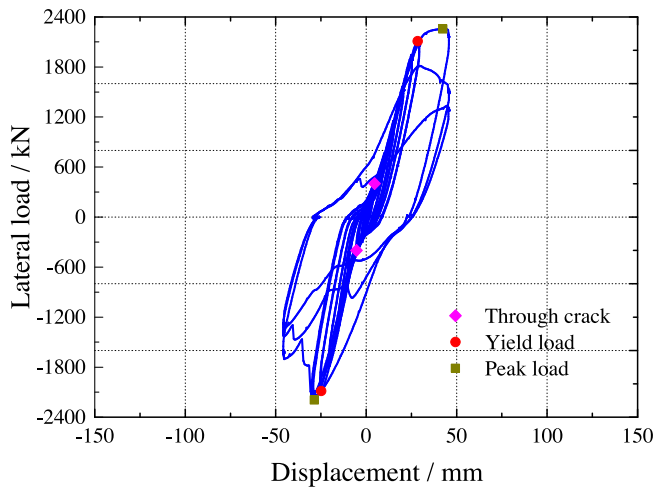
Fig. 13 shows the envelope curves of load-displacement response for test specimens, which were obtained by connecting the peak points under the first cycle of each loading level. These envelope curves illustrate that these specimens experienced elastic, elastic-plastic and failure stage. In the elastic stage, the relation between lateral load and displacement is almost linear, but the slope of these curves is different from each other, the initial stiffness increases with the decrease of shear-span ratio. In the elastic-plastic stage, the slope of envelope curve decreases nonlinearly. For test specimen CSW-3, it experienced a long elastic-plastic stage, the lateral load changes slightly with the increase of the displacement after ultimate loading, which shows good deformation capacity. However, the lateral load decreases abruptly after ultimate loading for test specimen CSW-1, and the ultimate displacement is much less than that for test specimen CSW-3. In the failure stage, the envelope curves show a decreasing trend, and both load-carrying capacity and rigidity decrease due to accumulated damage. For specimen CSW-1, there is a rapid descending stage without an obvious plastic period due to global buckling of the corrugated steel web, which experienced a brittle damage, thus, more attention should be paid to prevent global buckling of the corrugated steel web.

The ductility coefficient μ is used to evaluate the deformation capacity of test specimens, which is defined as the ratio of ultimate displacement to yield displacement as given in Eq. (1).

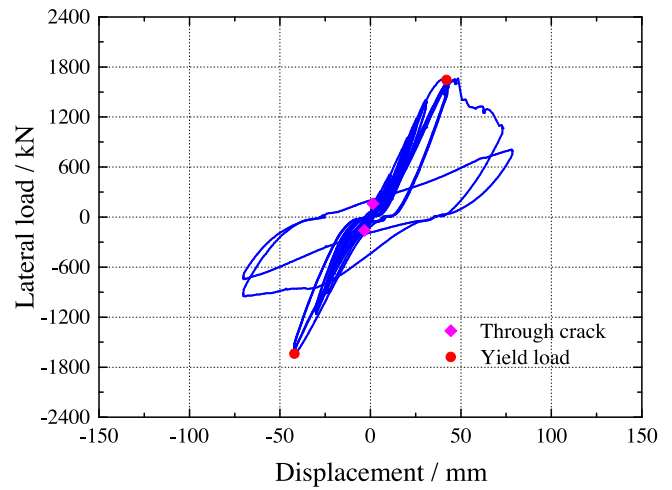
$$\mu = \Delta_u / \Delta_y \quad (1)$$

where, Δ_y is yield displacement corresponding to yield load F_y , which is determined by the general yield moment method [29], as shown in Fig. 14; Δ_u is ultimate displacement corresponding to ultimate load F_u , which is defined as lateral loading decreases to 85% of the peak load F_m . Table 3 summarizes the loads and corresponding displacements at critical states as well as the ductility coefficients of test specimens. For test specimen CSW-2, only yield load is available, while the measured peak load and ultimate load are not provided in the table due to unexpected welding fracture of the corrugated steel web, and the lateral load corresponding to the yielding of the longitudinal reinforcement was taken as the yield load.

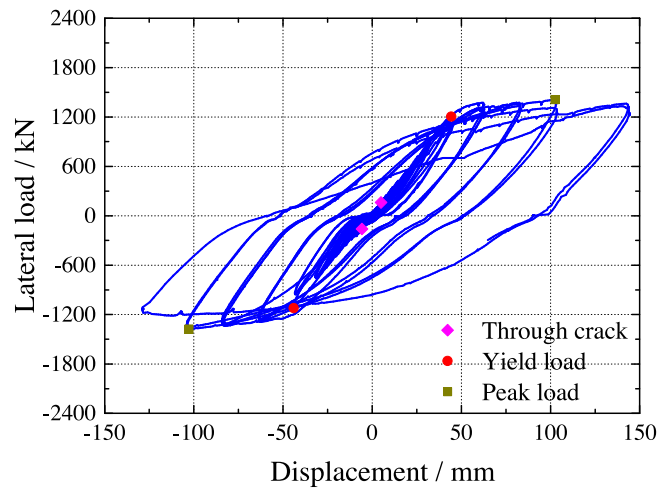
In comparison to test specimen CSW-3, the peak load of test specimen CSW-1 in positive and negative direction increase 60% and 59.5%, respectively, the load-carrying capacity decreases as the increase of shear-span ratio. Compared to specimen CSW-1, the yield displacement, ultimate displacement and ductility coefficient of test



(a) Specimen CSW-1



(b) Specimen CSW-2



(c) Specimen CSW-3

Fig. 12. Lateral load-displacement curves.

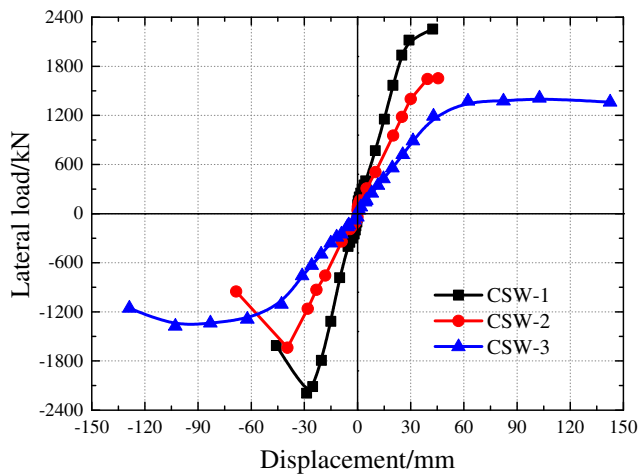


Fig. 13. Load-displacement envelope curves.

specimen CSW-3 are improved by an average value of 66.2%, 197% and 80.6% in positive and negative loading direction respectively. Therefore, the deformation capacity and ductility are enhanced significantly with the increase of shear-span ratio. The average ductility coefficient of test specimen CSW-1 is about 1.72, showing that the

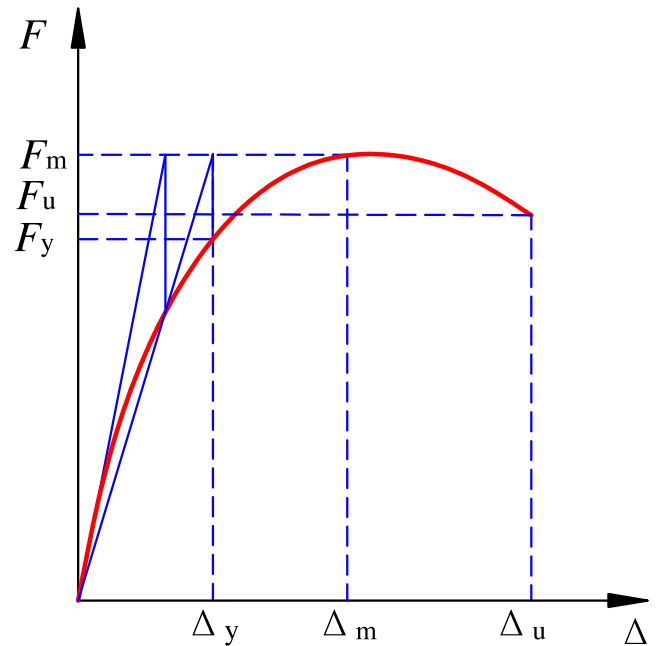


Fig. 14. General yield moment method.

Table 3
Load and displacement at different characteristic points.

Specimen	Loading direction	Yield point		Peak point		Ultimate point		Ductility coefficient/ μ
		F_y (kN)	Δ_y (mm)	F_m (kN)	Δ_m (mm)	F_u (kN)	Δ_u (mm)	
CSW-1	Positive	2109.3	28.5	2255.6	42.4	1499.6	45.7	1.60
	Negative	2086.9	24.9	2193.8	28.7	1611.9	45.8	1.84
CSW-2	Positive	1645.0	42.0	–	–	–	–	–
	Negative	1638.5	42.0	–	–	–	–	–
CSW-3	Positive	1204.9	44.3	1410.2	102.6	1239.1	143.8	3.24
	Negative	1122.2	44.0	1375.6	102.8	1155.4	128.7	2.92

plastic deformation capacity is poor. The average ductility coefficient of test specimen CSW-3 is about 3.08, indicating that the composite beam with corrugated steel webs of reasonable shear-span ratio exhibits good ductility.

4.3. Strength degradation

Strength degradation shows structural load-carrying capacity reduction with the increase of repeated loading cycles in the same displacement level. The strength degradation coefficient λ_i [30] is defined as the ratio of the peak load for i -th cycle to that for the first cycle at the same displacement level, as illustrated in Eq. (2).

$$\lambda_i = F_j^i / F_j^1 \tag{2}$$

where, i is the number of loading cycle; F_j^i is the peak load at the i -th loading cycle under displacement level j ; F_j^1 is the peak load at the first loading cycle under displacement level j .

Fig. 15 illustrates the variation of strength degradation coefficient (λ_2) with dimensionless displacement (Δ/Δ_y). In general, the strength degradation coefficients of these test specimens decrease with the increase of the displacement amplitude, the strength degradation coefficients are between 0.9 and 1.0 for test specimens CSW-2 and CSW-3 during the whole loading process, indicating that cyclic loading leads to strength deterioration in a slight degree. But, the strength degraded rapidly for test specimen CSW-1 after the peak load due to global buckling of the corrugated steel web, resulting in a brittle failure.

4.4. Stiffness degradation

Stiffness degradation reflects cumulative damage degree of the structure during repeated loading, and lateral stiffness K_j [30] of the test specimen under the same displacement level is defined as Eq. (3).

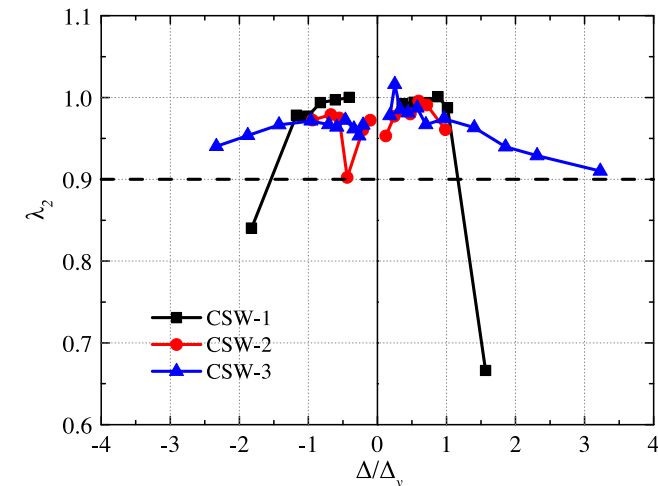


Fig. 15. Strength degradation curves.

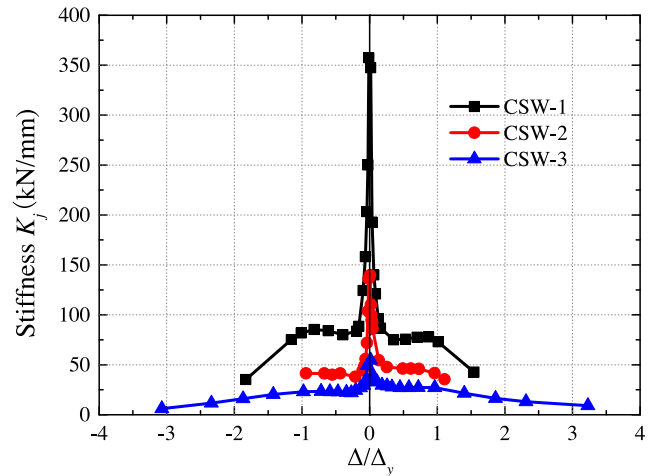


Fig. 16. Stiffness degradation curves.

$$K_j = \sum_{i=1}^n F_j^i / \sum_{i=1}^n \Delta_j^i \tag{3}$$

where, F_j^i is the peak load of the i -th loading cycle under the j -th displacement level; Δ_j^i is the corresponding displacement at the peak load F_j^i ; n is the number of loading cycles at the same displacement level.

The stiffness variation with dimensionless displacement (Δ/Δ_y) is depicted in Fig. 16. The stiffness degraded almost symmetrically in positive and negative direction during the cyclic loading process. The stiffness deteriorated significantly after concrete cracking initiation till through crack occurrence ($\Delta/\Delta_y < 0.25$), mainly due to the continuous propagation of concrete cracks and the increase of slippage at steel-concrete interface. From the stage of through crack occurrence to the yield of longitudinal reinforcements ($0.25 < \Delta/\Delta_y < 1$), the stiffness almost keep stable, since concrete cracks and slip at the steel-concrete interface were fully developed. After that, the stiffness decreases linearly and slightly till the specimen failure.

It can be found that the initial stiffness of test specimens decreases by increasing of shear-span ratio. When the lateral load was applied to through crack appeared, the stiffness of test specimen CSW-1 dropped to 23% of the initial stiffness, while the test specimens CSW-2 and CSW-3 degraded to 31% and 50%, respectively. From the stage of through crack occurrence to the yield of longitudinal reinforcements, the stiffness of test specimens CSW-1, CSW-2 and CSW-3 kept at about 80 kN/mm, 43 kN/mm and 27 kN/mm, respectively. After that, the stiffness of test specimen CSW-1 decreased rapidly, but the stiffness of test specimen CSW-2 reduced relative slowly. From the comparison of stiffness degradation curves, it can be concluded that the smaller the shear-span ratio, the greater the overall stiffness, also the higher rate of stiffness degradation.

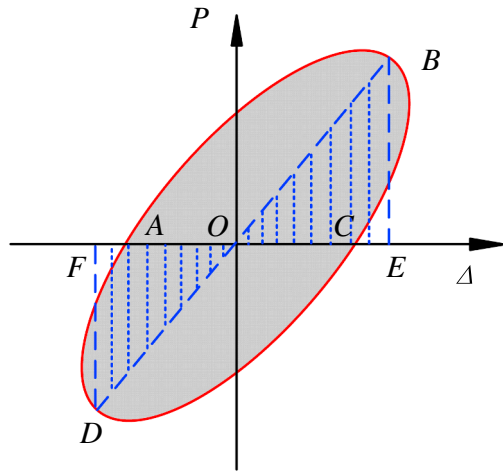


Fig. 17. Determination of equivalent viscous damping coefficient.

4.5. Energy dissipation capacity

As shown in Fig. 17, the energy dissipation capacity can be determined as the area surrounded by the hysteresis loops. At the same time, the energy dissipation capacity can also be evaluated by the equivalent viscous damping coefficient h_e [31], which is identified by Eq. (4).

$$h_e = \frac{1}{2\pi} \frac{S_D}{(S_{OBE} + S_{ODF})} \quad (4)$$

where, S_D is the energy dissipated by a hysteresis loop, defined as the area surrounded by the hysteretic curve, S_{OBE} and S_{ODF} are the energy dissipated by a linear elastic structure equivalent to the specimen, calculated by the areas of right-angled triangular OBE and ODF .

Fig. 18 shows the energy dissipated at the first loading cycle of each displacement level. In the elastic stage ($\Delta/\Delta_y < 1$), the dissipated energy of each specimen increases slowly, and the cumulated energy is below 30 kN·m. With the increase of applied displacement, concrete cracks appeared continuously and propagated through the section of concrete slab; plastic hinge was gradually formed and followed by the yielding of the test specimen. Accordingly, the dissipated energy increases rapidly, almost linearly with the dimensionless displacement Δ/Δ_y . At ultimate loading level, the energy dissipated by test specimen CSW-1 is 123 kN·m, and 308 kN·m by test specimen CSW-3, about 2.5 times of that by test specimen CSW-1, indicating that the energy dissipation capacity of the test specimen can be improved with the

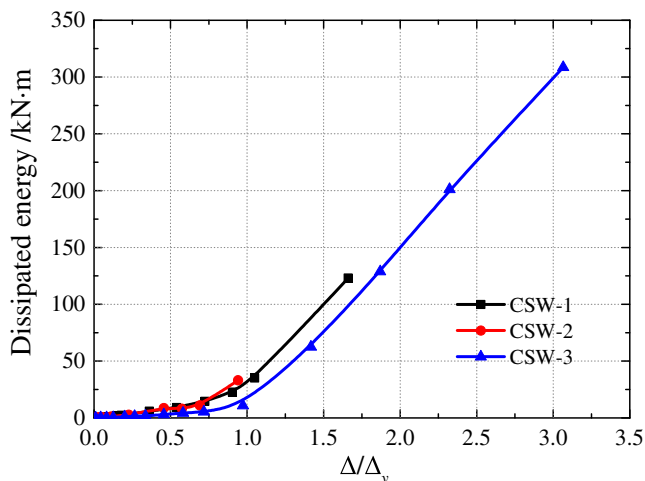


Fig. 18. Energy dissipation curves.

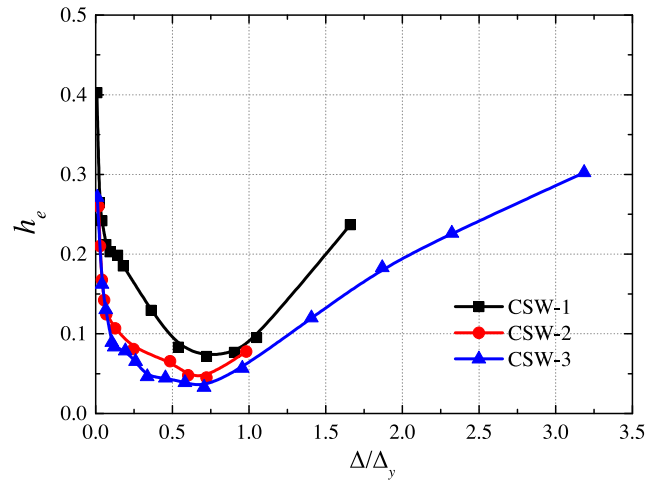


Fig. 19. Equivalent viscous damping coefficient curves.

increasing of shear-span ratio.

Fig. 19 illustrates the variation of equivalent viscous damping coefficients with the dimensionless displacement (Δ/Δ_y). The equivalent viscous damping coefficients decrease first and then increase with the increase of displacement amplitude, and the inflection point is near the yield point of test specimens. At initial loading stage, the bonding and friction between steel and concrete by shear connectors have not been destroyed. The connectors played a similar role as the damper, so the equivalent viscous damping coefficient is relatively large. With the increase of loading cycles, the bonding and friction gradually degraded resulting in the increase of relative slip between concrete and steel, therefore equivalent viscous damping coefficient decreased rapidly. When test specimen yield, the plastic deformation occurred, energy dissipation capacity was enhanced, and the equivalent viscous damping coefficient increased accordingly.

The equivalent viscous damping coefficients of test specimens CSW-1, CSW-2, and CSW-3 at yielding stage are 0.095, 0.078 and 0.053 respectively, while the damping ratio of steel and concrete composite structure is suggested to be 0.04 in Chinese Seismic Design Code of Building Structure (GB50011-2010) [32]. The equivalent viscous damping coefficients of specimens CSW-1 and CSW-3 at failure stage are 0.237 and 0.302, respectively. In general, the equivalent viscous damping coefficient at the failure stage is just between 0.1 and 0.2 for reinforced concrete (RC) structures [33]. From the aspect of equivalent viscous damping, it can be concluded that composite beams with corrugated steel webs have higher energy dissipation capacity than traditional RC structures do.

4.6. Deformation recovery ability

The deformation recovery ability is represented by residual deformation rate γ , which is defined as the ratio of residual displacement after unloading to the displacement corresponding to the peak load at each loading cycle, as given in Eq. (5):

$$\gamma = \frac{|\Delta_r^+| + |\Delta_r^-|}{|\Delta_m^-| + |\Delta_m^+|} \quad (5)$$

where, Δ_r^+ and Δ_r^- are the residual displacements in positive and negative direction after unloading at the same loading cycle; Δ_m^+ and Δ_m^- are the displacement corresponding to the peak load in the positive and negative direction at the same loading cycle. The variation of residual deformation rate with the applied dimensionless displacement (Δ/Δ_y) is depicted in Fig. 20.

With the increase of displacement amplitude, the residual deformation rate decreases first and then increases. Before the occurrence of through crack, the cohesion at the steel-concrete interface was

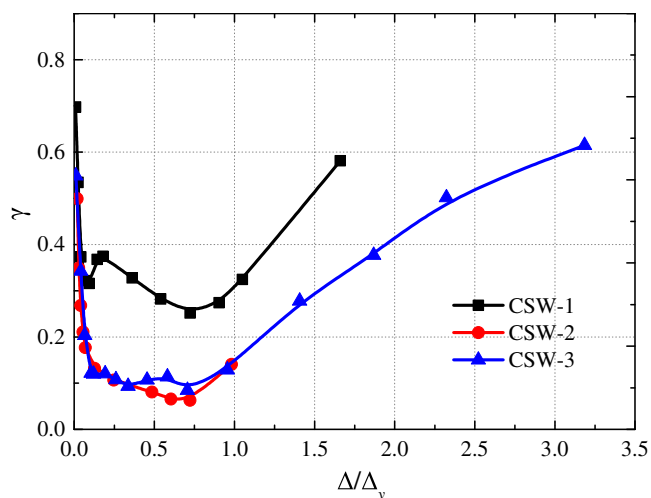


Fig. 20. Residual deformation rate curves.

continuously destroyed and relative slips were observed, moreover, the slip cannot be fully recovered after unloading, although residual deformation is small, the applied lateral displacement is also small, resulting in relatively large residual deformation rate. From the stage of through crack occurrence to the yield of longitudinal reinforcements, relative slip almost keeps stable; therefore the residual deformation rate is relatively reduced. However, from the stage of specimen yield to failure, plastic deformation continues to develop, and the residual deformation rate increases accordingly.

The residual deformation rate of test specimen CSW-1 is larger than that of specimens CSW-2 and CSW-3 during the loading process, which is mainly due to large relative slip between steel and concrete for specimen CSW-1 with smallest shear-span ratio. The residual deformation rates of specimens CSW-1 and CSW-3 at peak load are 0.32 and 0.50 respectively, while at ultimate load are about 0.6. The relatively small residual deformation rate shows test specimens having deformation recovery ability after the earthquake.

4.7. Shear force distribution

In the design of a composite beam with corrugated steel webs, the shear force is assumed to be carried entirely by the corrugated steel webs, and uniformly distributed along the web height [34]. However, Kadotani et al. [35] concluded that just 65% of the shear force was resisted by the corrugated steel webs. Because of the complicated boundary condition near the connection area, the contribution of corrugated steel web to shear may be different. Strain gauges were mounted to measure the shear distribution at concrete slabs and corrugated steel web, during the loading process, the test results are shown in Fig. 21.

The concrete slabs and the corrugated steel web each share a certain proportion of shear force. The concrete slabs carry a large portion of shear force near the fixed end due to the restraint against shear deformation of corrugated steel web; the proportion of the shear force resisted by the steel web is just about 30% in the elastic stage. The farther away from the fixed end, the more of the shear force carried by the steel web. With the increase of the applied lateral load, the contribution of corrugated steel web to shear increased with the propagation of cracking in concrete slabs; this behavior is obviously for Section 1-1 and 2-2 where near the fixed end of the composite beam. At the elastic-plastic stage, about 75–80% of the shear force was resisted by the corrugated steel web and the proportion remains nearly constant. At the ultimate state, the shear force carried by the steel web continued to increase because of severe cracking or crushing of the concrete slabs. However, the proportion decreased slightly after the buckling or

yielding of steel web in some sections.

4.8. Strain responses

During the loading process, strains on the longitudinal reinforcements and corrugated steel web were measured. Fig. 22 shows the variation of strains measured on the outermost longitudinal reinforcement with an applied lateral load for test specimen CSW-1 and CSW-3. The strain increases approximately linearly at the elastic stage, and the strain of longitudinal reinforcements in the tensile concrete slab is larger than that in the compression slab. The yield of longitudinal reinforcement occurs almost simultaneously as the specimen began to yield, which indicates that the yield of the test specimen is dominated by the yield of reinforced concrete slabs. In addition, test specimen CSW-3 failed in a flexure-dominating mode with a large strain of longitudinal reinforcement after yielding.

Fig. 23 shows the variation of shear strain responses of the corrugated steel web with an applied lateral load for test specimen CSW-1 and CSW-3. The shear strain increases approximately linearly during the loading process until the yielding of the steel web. The shear strains increase with the increase of the distance from the fixed end, indicating that the concrete slabs near the beam base carry more shear force. The shear strains keep approximately constant along the height of the web section, which indicates that the shear force distributes uniformly over the web and the stress in the corrugated web are almost pure shear stress. During the loading process, the steel web of test specimen CSW-3 was always in an elastic state, however, the steel web of test specimen CSW-1 yielded at the loading of 2000 kN, before shear buckling of the corrugated steel web, indicating that the specimen represented inelastic shear buckling failure mode.

5. Evaluation of the loading capacity

5.1. Flexural capacity

As discussed in previous sections, the specimen CSW-3 displayed a flexural failure mode, so the load-carrying capacity could be estimated by the flexural strength of the fixed end section of the composite beam. The following assumptions were made to evaluate the flexural capacity of the composite beam with corrugated steel web:

- (1) The relative slip between PBL connectors and concrete slabs are not considered, and the plane section remained plane after deformation [36].
- (2) The axial stiffness of the corrugated steel web was neglected due to the accordion effect. Hence, the bending moment is assumed to be resisted by the reinforcements, top and lower concrete flanges [37,38].
- (3) The tensile strength of cracked concrete is ignored. The extreme compressive fiber of concrete all reach the axial compressive strength f_c , the corresponding strain is taken to be 0.003 [39].
- (4) The stress-strain relationship of longitudinal reinforcements was idealized as an elastic-perfectly plastic model, the yield stress was used and the strain hardening effect was not considered for the reinforcements in tension. The strain of the reinforcements in compression was assumed to be the same as that of the concrete.
- (5) An equivalent rectangular compressive stress block with an average stress of $0.85f_c'$ and depth of βx is used to replace the more exact concrete stress distribution [39].
- (6) The contribution of the reinforcements within the extent of $0.5x$ from the neutral axis was neglected [40], since the stress of these reinforcements was not fully developed.

Fig. 24 shows the method for simplified evaluation of the flexural strength based on the above assumptions.

According to the force and moment equilibrium with respect to the

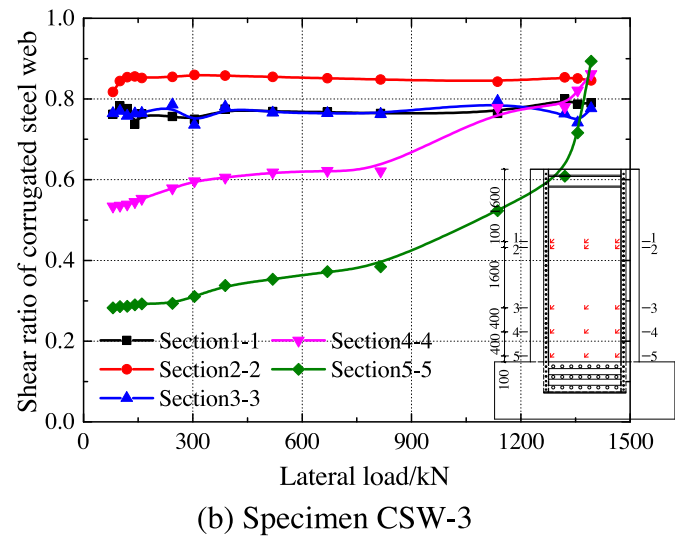
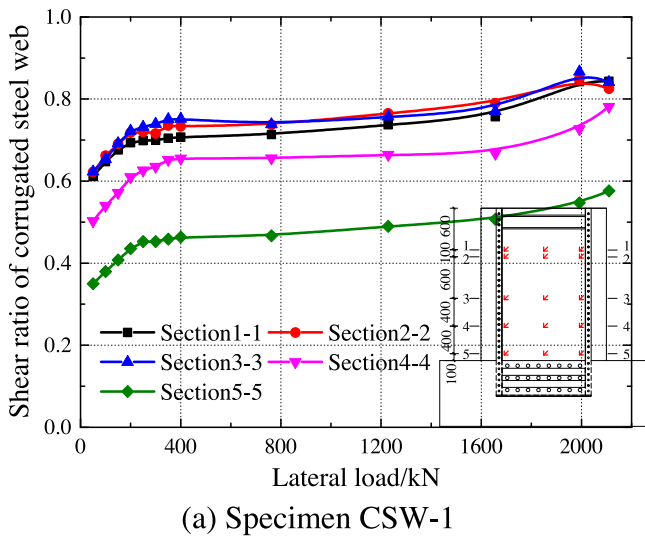


Fig. 21. Shear ratio of corrugated steel web.

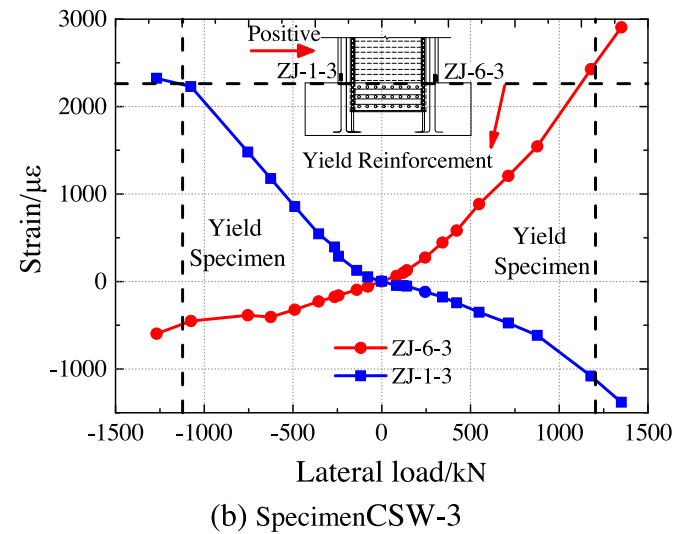
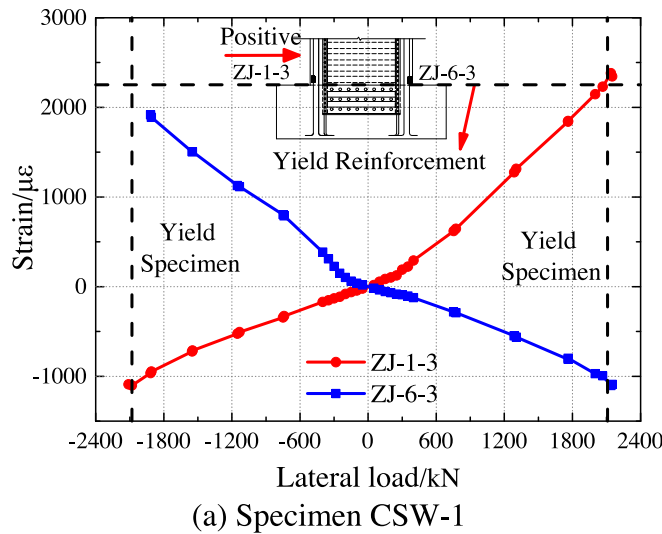


Fig. 22. Strains of longitudinal reinforcements.

neutral axis of the section, the following equations were established:

$$N_c = A_s f_s - A'_s f'_s \tag{6}$$

$$M_m = A_s f_s (0.5h - a_s) + A'_s f'_s (0.5h - a'_s) + 0.5N_c (h - \beta x) \tag{7}$$

$$N_c = 0.85\beta f'_c b_f x \tag{8}$$

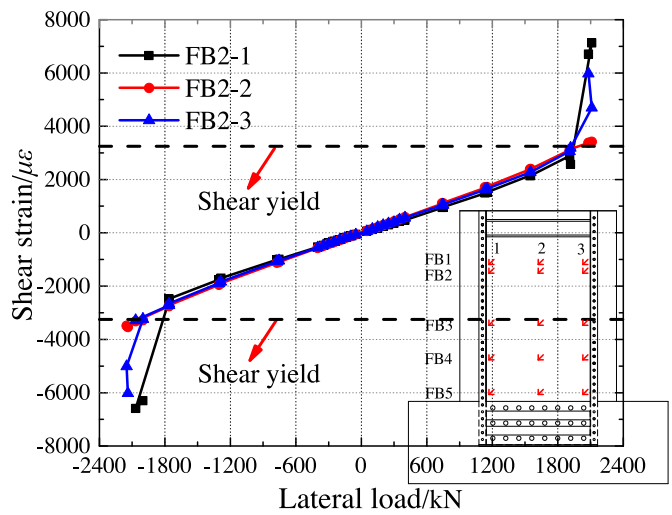
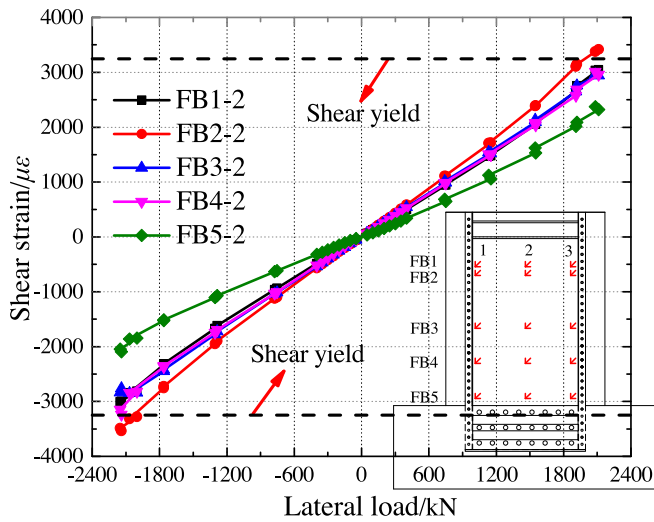
where, N_c denotes the reaction force of the concrete in compression; M_m represents the flexural strength of the beam section; A_s and A'_s are the cross-sectional areas of the reinforcements in tension and in compression, respectively; f_s and f'_s denote the tensile stress and compressive stress of the reinforcements, respectively; f'_c represents the cylinder compressive strength of the concrete, which can be calculated by $f'_c = 0.79f_{cu}$, f_{cu} denotes the cubic compressive strength; h and b_f are the depth of the composite beam and the width of the concrete slab, respectively; a_s and a'_s are the distances of the reinforcements centroid in tension and in compression to the nearest extreme concrete fiber, respectively; x denotes the distance from extreme compressive fiber to the neutral axis; the factor β defines the effective height of the compression zone, which should be taken as 0.85 for concrete with $f'_c \leq 28$ MPa and 0.05 less for each 7 MPa of f'_c in excess of 28 MPa, but β should not be taken less than 0.65 [39].

The evaluated flexural strength of test specimen CSW-3 is

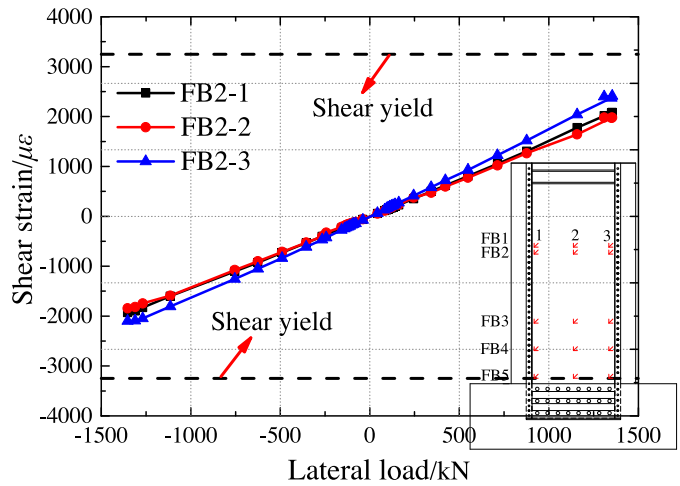
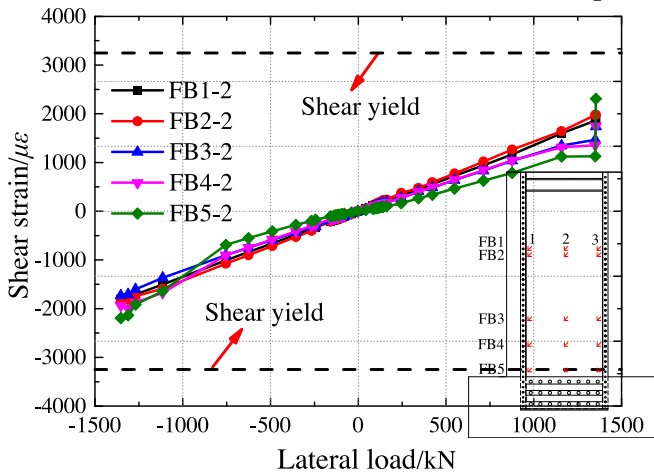
5956 kN m while the tested positive and negative load-carrying capacity is 5641 kN m and 5542 kN m, respectively. The calculated result is in good agreement with the test results, with a discrepancy of 0.06 and 0.08 in positive and negative direction, respectively. The simplified formulation slightly overestimated the load-carrying capacity, mainly because it was based on the structure that subjected to monotonic loading, the damage accumulated during the cyclic loading process was not concerned. As mentioned in Section 4.3, the cyclic loading will cause strength degradation, the tested loading capacity should be smaller than the calculated one. Therefore, the calculated result can only be used as the upper limit of flexural capacity and the reduction factors should be considered during the seismic design, but the exact values of these reduction factors still need to be further investigated.

5.2. Shear buckling capacity

As discussed in the previous sections, test specimen CSW-1 presented an inelastic shear buckling failure mode, the load-carrying capacity was controlled by the shear strength of the corrugated steel web. Shear buckling of the corrugated steel web often consists of global buckling or local buckling. Global buckling involves multiple folds and the buckled shape extends diagonally over the height of the web, while



(a) Specimen CSW-1



(b) Specimen CSW-3

Fig. 23. Strain responses of corrugated steel web.

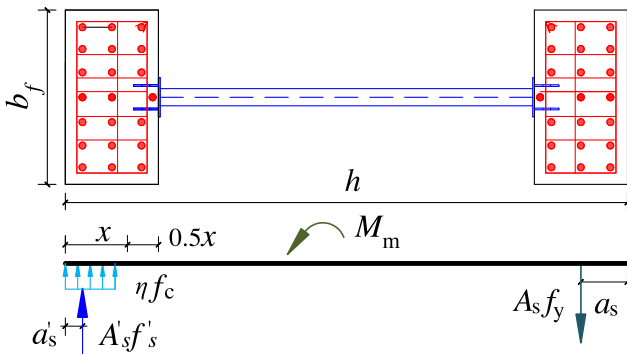


Fig. 24. Flexural strength evaluation of beam section.

local buckling represents a single flat panel. The local buckling deformations can also propagate into adjacent folds simultaneously.

The local elastic shear buckling stress of a corrugated steel web was derived from classic plate buckling theory [41]. A single plate was assumed to be supported by the adjacent folds and steel flanges. The corresponding local elastic shear buckling stress, $\tau_{cr,L}^e$ is:

$$\tau_{cr,L}^e = k_L \frac{\pi^2 E}{12(1 - \nu^2)} \left(\frac{t_w}{w} \right)^2 \quad (9)$$

where, E and ν are Young's modulus and Poisson's ratio respectively; w is the maximum panel width; t_w is the web thickness; k_L is the local shear buckling coefficient, assuming simply supported edges, k_L is given by $k_L = 5.34 + 4(w/h_w)^2$, in which h_w is the depth of the corrugated steel web.

An expression for the global elastic shear buckling stress of a corrugated steel plate, $\tau_{cr,G}^e$ was developed by Easley et al. [5] using the orthotropic plate theory:

$$\tau_{cr,G}^e = k_G \frac{D_y^{1/4} D_x^{3/4}}{t_w h_w^2} \quad (10)$$

where, k_G is the global shear buckling coefficient that depends on the boundary conditions. Easley et al. [5] proposed that k_G varies between 36 (assuming the web is simply supported by the flanges) and 68.4 (assuming that the flanges provide the web with fixed supports); D_x and D_y are the bending stiffnesses which are determined as follows:

$$D_x = \frac{Et_w^3 [(d/t_w)^2 + 1]}{6\eta} \quad (11)$$

$$D_y = \frac{Et_w^3}{12(1 - \nu^2)}\eta \tag{12}$$

where, d is the corrugation depth; and η is the length reduction factor, which is defined as $\eta = (a + b)/(a + c)$, in which a is the width of the horizontal plate, b and c are the projected and horizontal width of the inclined plate.

When the elastic shear buckling stress τ_{cr} exceeds 80% of the shear yield stress τ_y , the following inelastic equation provided by Elgaaly et al. [6] can be used to calculate the inelastic buckling stress:

$$\tau_{cr}^{in} = \sqrt{0.8\tau_y \tau_{cr}^e} \leq \tau_y \tag{13}$$

where, τ_y is determined using the von Mises yield criterion, $\tau_y = f_y/\sqrt{3}$.

Yi et al. [7] concluded that the buckling strength of the corrugated steel web is controlled by interactive buckling which is attributed to the interaction between local and global shear buckling modes, and proposed the calculation method of elastic interactive shear buckling stress $\tau_{cr,I}^e$.

$$\frac{1}{\tau_{cr,I}^e} = \frac{1}{\tau_{cr,L}^e} + \frac{1}{\tau_{cr,G}^e} \tag{14}$$

The shear strength of corrugated steel web considering material inelasticity, residual stress, and initial imperfections, can be determined from the following buckling curve [42], and the buckling curve is adopted from the design manual for PC bridges with corrugated steel webs [43].

$$\frac{\tau_n}{\tau_y} = \begin{cases} 1 & \lambda_s < 0.6 \\ 1 - 0.614(\lambda_s - 0.6) & 0.6 \leq \lambda_s \leq \sqrt{2} \\ 1/\lambda_s^2 & \sqrt{2} < \lambda_s \end{cases} \tag{15}$$

where, τ_n is the shear buckling strength, λ_s is the slenderness parameter of the web under shear, $\lambda_s = \sqrt{\tau_y/\tau_{cr,I}^e}$.

Driver et al. [10] proposed the following formula to predict the shear strength of corrugated steel webs in bridge girders; this equation covers inelastic buckling and shear yielding:

$$\frac{1}{(\tau_n)^2} = \frac{1}{(\tau_{cr,L})^2} + \frac{1}{(\tau_{cr,G})^2} \tag{16}$$

where, $\tau_{cr,L} = \tau_{cr,L}^e$ if $\tau_{cr,L}^e \leq 0.8\tau_y$ and $\tau_{cr,L} = \tau_{cr,L}^{in}$ otherwise, and $\tau_{cr,G} = \tau_{cr,G}^e$ if $\tau_{cr,G}^e \leq 0.8\tau_y$ and $\tau_{cr,G} = \tau_{cr,G}^{in}$ otherwise.

El-Metwally [11] suggested another formula to calculate the shear strength including the shear yield stress τ_y , as illustrated in Eq. (17).

$$\frac{1}{(\tau_n)^2} = \frac{1}{(\tau_{cr,L}^e)^2} + \frac{1}{(\tau_{cr,G}^e)^2} + \frac{1}{(\tau_y)^2} \tag{17}$$

Sauce and Braxtan [12] summarized a large number of previous test results and derived a similar formula to calculate the shear strength, as shown in Eq. (18).

$$\frac{1}{(\tau_n)^3} = \frac{1}{(\tau_{cr,L}^e)^3} + \frac{1}{(\tau_{cr,G}^e)^3} + \frac{2}{(\tau_y)^3} \tag{18}$$

Hassanein and Kharoob [44] believed that the boundary conditions between the corrugated steel web and the top/bottom flanges are close to fixed conditions, and proposed Eq. (19) to calculate shear capacity under such boundary conditions.

$$\frac{1}{(\tau_n)^3} = \frac{(\tau_{cr,L}^e)^3(\tau_{cr,G}^e)^3}{[(\tau_{cr,L}^e)^{0.6} + (\tau_{cr,G}^e)^{0.6}]^3} + \frac{2}{(\tau_y)^3} \tag{19}$$

As shown in the test results, the shear stress approximately keeps constant along the height of the web section. So, the shear force V of corrugated steel web can be evaluated as follows:

$$V = \tau_n h_w t_w \tag{20}$$

Table 4
Calculated and measured shear buckling strength of test specimen CSW-1.

Formulas	V_{cal} (kN)	V_{exp} (kN)	V_{cal}/V_{exp}
Yi et al.	1697	1755	0.97
Driver et al.	1235	1755	0.70
El-Metwally	1652	1755	0.94
Sauce & Braxtan	1377	1755	0.78
Hassanein & Kharoob	1380	1755	0.79

of test specimen CSW-1 using the above-mentioned formulas. In addition, the comparison of the test shear strength (V_{exp}) to the calculated ones (V_{cal}) is also shown in Table 4. As we can see, the formulas proposed by Driver et al. [10], Sauce & Braxtan [12], and Hassanein & Kharoob [44] are too conservative. The formula suggested by El-Metwally [11] was less conservative with a discrepancy of 0.06. The analytical result calculated by formulas proposed by Yi et al. [7] agrees well with the test result, the discrepancy is just 0.03. Therefore, the formulas proposed by Yi et al. [7] are suggested to predict the shear strength of the corrugated steel web in composite beams which presented shear buckling failure.

6. Conclusions

An innovative application of corrugated steel plates as the webs of crossbeams in suspension bridge tower was proposed in this study. Quasi-static tests on three composite beams with corrugated steel web of different shear-span ratios were conducted to investigate their cyclic behavior, and related conclusions can be obtained as follows:

- (1) Due to different shear-span ratio, the failure modes of test specimens include shear buckling of corrugated steel web, welding fracture or flexural failure. For test specimen CSW-1 with the smallest shear-span ratio, corrugated steel web buckled in an “X” shape, and concrete slabs produced longitudinal split cracks. Test specimen CSW-2 experienced an unexpected welding fracture, and longitudinal cracks of CSW-2 occurred similar to that of CSW-1. For test specimen CSW-3 with the largest shear-span ratio, concrete crushing and buckling of longitudinal reinforcements were observed, showing typical flexural failure mode.
- (2) The hysteretic curve is plump with slight pinching and the ductility coefficient is more than 3 for test specimen CSW-3, indicating good energy dissipation and deformation capacity. However, the hysteretic curve is less plentiful with obvious pinching phenomenon for CSW-1, showing relative poor seismic performance. The energy dissipation capacity of test specimens is better than that of RC structures, the strength degradation is not obvious and the deformation recovery ability is good for all test specimens.
- (3) With the decrease of shear-span ratio, the load-carrying capacity and elastic stiffness of test specimens are increased, while the ductility coefficient is decreased, the degradation rate of stiffness is accelerated. Application of composite beam with small shear-span ratio should be considered carefully.
- (4) The corrugated steel web just carries about 30% of the shear force at the fixed end in the elastic stage, the farther away from the fixed end, the more of shear force carried by the steel web, which is up to about 80% in the elastic-plastic stage. The shear force distributes uniformly over the web height and the stress in the corrugated web is almost pure shear stress.
- (5) The simplified formulas were developed to evaluate the flexural strength of the composite beam with a discrepancy less than 10%. Different formulas for calculating the shear strength of corrugated steel web were compared with the test results, the formulas proposed by Yi et al. [7] are suggested to predict the shear strength of the corrugated steel web with high accuracy.
- (6) This paper focused on the experimental studies on the cyclic

Table 4 shows the calculated shear strength of corrugated steel web

behavior of composite beams with corrugated steel webs considering different shear-span ratios, other factors (such as corrugation profile, material properties and so on) affecting the cyclic behavior will be further investigated experimentally and numerically.

Acknowledgments

This research is supported by the National Nature Science Foundation of China (Grant No. 51308070). The authors wish to express their gratitude to the sponsor.

References

- [1] He J, Liu Y, Chen A, Yoda T. Mechanical behavior and analysis of composite bridges with corrugated steel webs: state-of-the-art. *Int J Steel Struct* 2012;12(3):321–38.
- [2] Tao Q, Cao F, Jiang J, Liu Z. Key Techniques of seismic design of Xingkang Dadu River Bridge in Luding. *Bridg Constr* 2018;48:90–5. [in Chinese].
- [3] Wang S, He J, Liu Y, Li C, Xin H. Shear capacity of a novel joint between corrugated steel web and concrete lower slab. *Constr Build Mater* 2018;163:360–75.
- [4] He J, Liu Y, Chen A, Wang D, Yoda T. Bending behavior of concrete-encased composite I-girder with corrugated steel web. *Thin-Walled Struct* 2014;74:70–84.
- [5] Easley JT. Buckling formulas for corrugated metal shear diaphragms. *J Struct Div ASCE* 1975;101(7):1403–17.
- [6] Elgaaly M, Hamilton RW, Seshadri A. Shear strength of beams with corrugated webs. *J Struct Eng ASCE* 1996;122(4):390–8.
- [7] Yi J, Gil H, Youm K, Lee H. Interactive shear buckling behavior of trapezoidally corrugated steel webs. *Eng Struct* 2008;30(6):1659–66.
- [8] Elkawas AA, Hassanein MF, Elchalakani M. Lateral-torsional buckling strength and behaviour of high-strength steel corrugated web girders for bridge construction. *Thin-Walled Struct* 2018;122:112–23.
- [9] He J, Liu Y, Xu X, Li L. Loading capacity evaluation of composite box girder with corrugated webs and steel tube slab. *Struct Eng Mech* 2014;50(4):501–24.
- [10] Driver RG, Abbas HH, Sause R. Shear behavior of corrugated web bridge girders. *J Struct Eng ASCE* 2006;32(2):195–203.
- [11] El-Metwally AS. Prestressed composite girders with corrugated steel webs MS. thesis University of Calgary: Calgary (AB): Dept. of Civil Engineering; 1998.
- [12] Sause R, Braxtan TN. Shear strength of trapezoidal corrugated steel webs. *J Constr Steel Res* 2011;67:223–36.
- [13] He J, Liu Y, Chen A, Yoda T. Shear behavior of partially encased composite I-girder with corrugated steel web: experimental study. *J Constr Steel Res* 2012;77:193–209.
- [14] He J, Liu Y, Chen A, Yoda T. Shear behavior of partially encased composite I-girder with corrugated steel web: numerical study. *J Constr Steel Res* 2012;79:166–82.
- [15] He J, Wang S, Liu Y, Lyu Z, Li C. Mechanical behavior of partially encased composite girder with corrugated steel web: interaction of shear and bending. *Engineering* 2017;3(6):806–16.
- [16] Jáger B, Dunai L, Kövesdi B. Flange buckling behavior of girders with corrugated web part I: experimental study. *Thin-Walled Struct* 2017;118:181–95.
- [17] Kövesdi B, Dunai L. Fatigue life of girders with trapezoidally corrugated webs: an experimental study. *Int J Fatigue* 2014;64:22–32.
- [18] Mo YL, Perng SF. Behavior of framed shear walls made of corrugated steel under lateral load reversals. *Adv Struct Eng ASCE* 2000;3(3):255–62.
- [19] Shimizu N, Kanno R, Ikarashi K, Sato K, Hanya K. Cyclic behavior of corrugated steel shear diaphragms with end failure. *J Struct Eng* 2013;139(5):796–806.
- [20] Emami F, Mofid M, Vafai A. Experimental study on cyclic behavior of trapezoidally corrugated steel shear walls. *Eng Struct* 2013;48:750–62.
- [21] Emami F, Mofid M. On the hysteretic behavior of trapezoidally corrugated steel shear walls. *Struct Des Tall Spec Build* 2014;23(2):94–104.
- [22] Bahrebar M, Kabir MZ, Zirakian T, Hajsadeghi M, Lim JBP. Structural performance assessment of trapezoidally-corrugated and centrally-perforated steel plate shear walls. *J Constr Steel Res* 2016;122:584–94.
- [23] Farzampour A, Laman JA, Mofid M. Behavior prediction of corrugated steel plate shear walls with openings. *J. Constr. Steel Res* 2015;114:258–68.
- [24] Aydın R, Yuksel E, Yardımcı N, et al. Cyclic behaviour of diagonally-stiffened beam-to-column connections of corrugated-web I sections. *Eng Struct* 2016;121:120–35.
- [25] Aydın R, Yuksel E, Yardımcı N, et al. In-plane behaviour of beam-to-column connections of corrugated web I-sections. *J Constr Steel Res* 2014;100:183–96.
- [26] Shahmohammadi A, Mirghaderi R, Hajsadeghi M, et al. Application of corrugated plates as the web of steel coupling beams. *J. Constr. Steel Res* 2013;85:178–90.
- [27] Hajsadeghi M, Zirakian T, Keyhani A, Naderi R, Shahmohammadi A. Energy dissipation characteristics of steel coupling beams with corrugated webs. *J Constr Steel Res* 2014;101:124–32.
- [28] CMC. Code for Design of Concrete Structures (GB 50010-2010). Beijing: China Ministry of Construction; 2010. [in Chinese].
- [29] Zhao B, Zhou T, Chen Z, et al. Experimental seismic behavior of SCFRP column chevron concentrically braced frames. *J Constr Steel Res* 2017;133:141–55.
- [30] Wang B, Jiang H, Lu X. Experimental and numerical investigations on seismic behavior of steel truss reinforced concrete core walls. *Eng Struct* 2017;140:164–76.
- [31] Ramírez P, Sandoval C, Almazán JL. Experimental study on in-plane cyclic response of partially grouted reinforced concrete masonry shear walls. *Eng Struct* 2016;126:598–617.
- [32] CMC. Code for Seismic Design of Buildings (GB 50011-2010). Beijing: Ministry of Housing and Urban-Rural Development of China; 2011. [in Chinese].
- [33] Xue J, Ma H, Liu Y. Experimental study on seismic performance of steel reinforced recycled concrete columns under low-cyclic reversed loading. *China Civ Eng J* 2014;1:36–46. (in Chinese).
- [34] Johnson RP, Cafolla J. Corrugated webs in plate girders for bridges corrugated webs in plate girders for bridges. *Proc Inst Civ Eng Struct Build* 1997;122(2):157–64.
- [35] Kadotani T, Aoki K, Ashizuka K, Mori T, Tomimoto M, Kano M. Shear buckling behavior of prestressed concrete girders with corrugated steel webs. *Proc., 1st fib Congress, Session 5: Composite Structures Osaka, Japan. 2002.* p. 269–76.
- [36] Yamaguchi K, Yamaguchi T, Ikeda S. The mechanical behavior of composite prestressed concrete girders with corrugated steel webs. *Concr Res Technol JCI* 1997;8(1):27–40. [in Japanese].
- [37] Jiang R, Au FTK, Xiao Y. Prestressed concrete girder bridges with corrugated steel webs: review. *J Struct Eng* 2015;141(2):1–9. 04014108.
- [38] Metwally AE, Loov RE. Corrugated steel webs for prestressed concrete girders. *RILEM Mater Struct* 2003;36(3):127–34.
- [39] Building Code ACI. Requirements for Structural Concrete and Commentary (ACI 318-05). Farmington Hills: American Concrete Institute; 2005.
- [40] Qian J, Jiang Z, Ji X. Behavior of steel tube-reinforced concrete composite walls subjected to high axial force and cyclic loading. *Eng Struct* 2012;36(3):173–84.
- [41] Timoshenko SP, Gere JM. *Theory of Elastic Stability*. 2nd ed. New York: McGraw-Hill; 1961.
- [42] Moon J, Yi J, Choi BH, Lee H. Shear strength and design of trapezoidally corrugated steel webs. *J Constr Steel Res* 2009;65:1198–205.
- [43] Research committee for hybrid structures with corrugated steel web, Design manual for PC bridges with corrugated steel webs; 1998 [in Japanese].
- [44] Hassanein MF, Kharoob OF. Behavior of bridge girders with corrugated webs: (II) shear strength and design. *Eng Struct* 2013;57:544–53.